JOURNAL OF PROPULSION AND POWER
Vol. 15, No. 6, November–December 1999

Internal Ballistics Considerations of Nozzleless Rocket Motors

Alon Gany*
Princeton University, Princeton, New Jersey 08544
and
Israel Aharon†
Technion—Israel Institute of Technology, 32000 Haifa, Israel

The fundamentals of the internal ballistics of solid-propellant nozzleless rocket motors have been studied theoretically and experimentally. Aimed at the major basic aspects, the theoretical analysis consisted of a quasi-steady-state one-dimensional flow of a perfect gas in a constant-area port, assuming a uniform burning rate along the grain as a result of the compensating effects of erosive and pressure-dependent burning contributions. The simplified analysis has been found to be an excellent tool to exhibit fundamental characteristics. It revealed that the theoretical achievable specific impulse in a nozzleless rocket cannot exceed approximately 86% of its value in an adapted-nozzle rocket operating at the same average chamber pressure. An experimental parametric study using cylindrical propellant grains has demonstrated good agreement with the major parameters addressed in the theoretical analysis, indicating that the assumption of a uniform burning rate is a realistic approximation.

Nomenclature

A_b = burning area
A_p = port cross-sectional area
a = constant in the burning-rate law, Eq. (1); speed of sound
C = constant, Eq. (4)
C_F = thrust coefficient
C_F° = thrust coefficient of adapted nozzle
c_p = specific heat
c^* = characteristic velocity
D = port diameter
F = motor thrust
f = frequency
g_0 = standard gravity acceleration
h = enthalpy (per unit mass)
I_{sp} = specific impulse
L = grain length
L^* = characteristic length
M = Mach number
m = mass
$\dot{m}$ = mass flow rate
n = pressure exponent in burning-rate law, Eq. (1)
p = pressure
R = specific gas constant
$\dot{r}$ = propellant burning rate
T = temperature
t = time
u = axial velocity
x = distance along the grain
Γ = function of γ, Eq. (8)
γ = specific heat ratio
λ = diameter ratio
ρ = density

Subscripts

a = ambient
av = average
b = burning; burnout
e = exit plane
i = initial
max = maximum
N = nozzled
NL = nozzleless
p = propellant
t = total (stagnation) properties
0 = head-end conditions

Superscript

$\bar{}$ = average

Presented as Paper 95-2735 at the AIAA/ASME/SAE/ASEE 31st Joint Propulsion Conference, San Diego, CA, 10–12 July 1995; received 27 July 1995; revision received 21 October 1998; accepted for publication 16 August 1999.

*Visiting Professor, Department of Mechanical and Aerospace Engineering, on sabbatical leave from the Technion; currently Professor and Head, Fine Rocket Propulsion Center, Faculty of Aerospace Engineering, Technion—Israel Institute of Technology, 32000 Haifa, Israel; gany@aerodyne.technion.ac.il. Associate Fellow AIAA.

†Graduate Student, Faculty of Aerospace Engineering; currently Chief Research Engineer, P.O. Box 2250, Ballistics and Explosives Department, Rafael, 31021 Haifa, Israel. Member AIAA.

Introduction

NOZZLELESS solid rocket motors (NSRMs) are characterized by the absence of a nozzle at the aft end of the motor. Their solid-propellant grain is usually a cylindrical perforation (Fig. 1). The simplicity, reliability, and cost effectiveness due to the avoidance of a nozzle, the simple propellant configuration, and the reduced insulation requirements make the NSRM an attractive concept in spite of its lower specific impulse (by about 20%) compared to nozzled motors.[1] In addition, the elimination of the nozzle assembly is used to increase the overall amount of propellant that, in most instances, can compensate for the reduced performance. Nozzleless solid-propellant motors seem to be of particular interest for applications to integral-rocket-ramjet boosters because of their better volumetric efficiency and the avoidance of ejectable nozzle assembly.[2]

Because of the specific operating regime, nozzleless rocket propellants are typically characterized by better mechanical properties and higher burning rates.

Fundamental solutions of quasi-one-dimensional adiabatic flow with mass addition in a constant-area duct have been employed for performance calculations of cylindrical solid-propellant motors, with some implications to nozzleless rocket motors.[3–5] Influences due to departure from one dimensionality on the flowfield development and choking conditions have been studied analytically. Glick and Orr[6] and Glick[7] demonstrated that the radial profile of the axial velocity leads to a choking plane with a nonuniform Mach number.

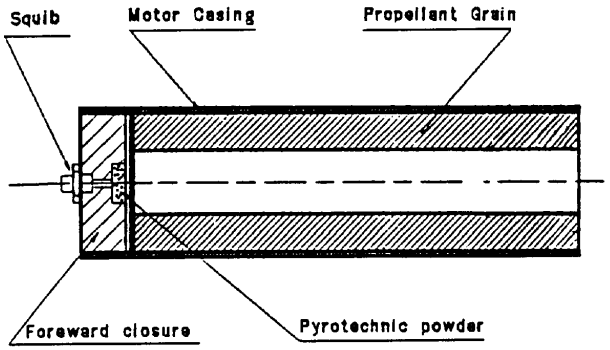

Fig. 1 Schematic of a nozzleless solid-propellant motor.

In Refs. 6 and 7, it was concluded that two-dimensional effects should yield a performance increment of about 4–5% over the one-dimensional predictions. Later, experiments by Traineau et al.[8] and an analysis by King[9] revealed a much smaller effect, less than 2%, apparently because the radial distribution of the axial velocity is flatter than previously expected. The more recent analysis by Balakrishnan et al.[10] predicted some 3–4% improvement in the vacuum specific impulse when assuming a frictionless, rotational flow.

A database has been provided by a number of experimental investigations,[2,11–13] enabling the examination of different theoretical assumptions and solutions.

One of the most significant phenomena in nozzleless rockets is erosive burning causing enhancement of the propellant burning rate in the case of high-speed crossflow in comparison to stagnant conditions. Because the flow in a nozzleless motor accelerates from practically zero velocity at the head end to sonic and sometimes supersonic speeds at the exit zone, one expects that increasing erosive-burning effects will be encountered for increasing distances along the grain. The phenomena associated with the origin and effects of erosive burning have been discussed and modeled in numerous articles.[10,14–19] It is generally accepted that among the major factors influencing the erosive burning are Mach number, Reynolds number, and turbulence intensity, and that these effects are much more pronounced in nozzleless motors than in nozzled solid rockets.

Other influences that cannot readily be incorporated in a simple analytical solution are grain deflection,[20] two-phase flow effects, and combustion efficiency.[21] The former effect results from the direct influence of grain deformation on the choking cross section, whereas the latter are of concern in the case of propellants containing aluminum (or other metal) particle additives.

In our opinion, analytical studies would yield a good physical insight on fundamental performance characteristics and influencing parameters in nozzleless rockets. Unfortunately, this powerful tool has not been fully exploited because such studies were replaced by a technical approach in a relatively early stage. Precise prediction requirements for engineering purposes have led to the development of numerical codes on the internal ballistics of nozzleless rocket motors,[2,11,19,22–24] incorporating the different effects in empirical or semi-empirical manners, with the major concern being the simulation of the two main measurable parameters, namely, head pressure and thrust vs time. Such programs usually involved a large number of adjustable constants and parameters (Ref. 2 quotes as many as 15 parameters).

A one-dimensional analysis seems to account for the most influencing factors in a reasonable physical manner, highlighting the fundamental nozzleless rocket performance characteristics. Because turbulence and viscous effects play an essential role in the erosive-burning phenomena, one may argue that the one-dimensional model can be a better physical approximation than a rotational, inviscid flow description. The one-dimensional analysis may also serve as an excellent preliminary design tool, as well as for initial safety assessment (prediction of peak pressure and thrust).

The objective of this investigation is to carry out an explicit one-dimensional analysis of the internal ballistics of nozzleless rocket motors and to relate and compare the analytical findings to systematic parametric results obtained from a parallel experimental effort.

Analysis

The analysis assumes a quasi-steady one-dimensional frictionless gas flow in a constant-area duct with distributed mass addition along the wall. As the chemical reaction (and heat release) in solid-propellant combustion is accomplished within a very short distance from the wall, one can consider the core flow as adiabatic and nonviscous. The assumptions of constant physical gas properties, for example, molecular weight, specific heat c_p, and specific heat ratio γ, as well as quasi-steady flow along the combustor in spite of the continuous regression of the propellant surface, provide a good first-order approximation in solid-propellant motors.

Assuming that the flow properties are a function of the distance along the combustor and are uniform at a cross section implies that the flow attains Mach number of unity and choking conditions at the end of the constant-area duct. As mentioned before, not accounting for two-dimensional effects implies only second-order underestimation of motor performance, generally within the inaccuracy introduced by the other common assumptions.

The most significant physical approximation that is incorporated in this model and that should make its predictions more realistic than those of other analytical models is the view that the propellant burning rate is practically uniform along the grain at any time instance. In a way, this accounts for the erosive-burning phenomenon, which is consistent with the physical trend of this effect, whose magnitude increases in the downstream direction, compensating for the decreasing pressure-dependent contribution of the burning rate. The use of a uniform burning rate along the grain exhibits good agreement (within few percent) with the experimental findings of Nahon[11] and Traineau and Kuentzmann,[12] as well as with this study. As a general rule, it seems to offer a good approximation for common grain geometries. Deviations from the simplified model may be expected for very large diameter motors (due to smaller erosive burning effects) or for very high L/D motors (due to higher grain deflection and erosive-burning effects).

The instantaneous burning rate $\dot{r}$ is, thus, represented by its value at the head end, which is a function of the head-end pressure p_0 alone, because there is no crossflow there:

$$\dot{r} = ap_0^n \tag{1}$$

The governing one-dimensional conservation equations of mass, momentum, and energy in the constant area port are, respectively: $\mathrm{d}\dot{m} = A_p\,\mathrm{d}(\rho u)$, $-\mathrm{d}p = \mathrm{d}(\rho u^2)$, and $\mathrm{d}h + u\,\mathrm{d}u = 0$. Assuming a perfect gas implies the equation of state $p = \rho RT$ and the specific heat expression $c_p = \gamma R/(\gamma - 1)$, where R is the specific gas constant. One can readily show that, when using the choking condition $M = 1$ at the downstream end of the motor (exit plane, indexed e), the following relationships can be obtained:

$$T_e = 2T_0/(\gamma + 1), \qquad T_{te} = T_0 \tag{2}$$

$$p_e = p_0/(\gamma + 1), \qquad p_{te} = \tfrac{1}{2}[(\gamma + 1)/2]^{1/(\gamma - 1)}p_0 = Cp_0 \tag{3}$$

As expected, the total (stagnation) temperature remains constant along the entire motor as a result of the constant total enthalpy. However, the constant C

$$C = \tfrac{1}{2}[(\gamma + 1)/2]^{1/(\gamma - 1)} \tag{4}$$

which is very close to 0.8 (within ±1%) for typical values of γ, demonstrates stagnation pressure loss of some 20% along the grain. This loss results from the nonisentropic conditions associated with mass addition at increasing entropy levels (due to the decreasing pressure) along the grain. The head-end pressure is the highest pressure in the motor at any moment, whereas, in general, head-end properties represent stagnation conditions because of the zero flow velocity.

By the integrating of the mass and momentum equations along the grain, and by the using of the boundary conditions $\dot{m} = 0$ and $p = p_0$ at the head end ($x = 0$), one obtains (see elaboration by Price[3])

$$p/p_0 = \frac{\left\{1 + \gamma\left[1 - (\dot{m}/\dot{m}_e)^2\right]^{\frac{1}{2}}\right\}}{(1+\gamma)} \tag{5}$$

where p and $\dot{m}$ are, respectively, the static pressure and mass flow rate at some axial distance along the grain and $\dot{m}_e$ is the overall mass flow rate at the exit plane, which is considered the choking location ($M_e = 1$). Because, according to our assumption, the instantaneous burning rate $\dot{r}$ is uniform along the grain, then the relative mass flow rate at any axial location is equal to its relative distance along the grain; hence,

$$p/p_0 = \frac{\left\{1 + \gamma\left[1 - (x/L)^2\right]^{\frac{1}{2}}\right\}}{(1+\gamma)} \tag{6}$$

Interestingly, from their tests Traineau et al.[8] concluded that pressure ratio can be predicted more accurately by one-dimensional than by two-dimensional calculations if viscous and irreversibility effects are not accounted for.

The energetic performance of the combustion chamber can be expressed by the commonly used characteristic velocity c^*, whose thermodynamic expression remains as in nozzled rockets

$$c^* = 1/\Gamma\sqrt{RT_0} \tag{7}$$

where T_0 is the constant stagnation temperature in the chamber and Γ is defined as

$$\Gamma = \sqrt{\gamma}[2/(\gamma+1)]^{(\gamma+1)/2(\gamma-1)} \tag{8}$$

However, the application of c^* to mass flow rate calculations should be related to the aft-end total pressure

$$\dot{m} = p_{te}A_p/c^* \tag{9}$$

where A_p, the port cross section, also represents the throat (or choking) and exit cross sections. When using the measurable head-end pressure p_0 (p_e or p_{te} are not regularly measured quantities), one finds that

$$\dot{m} = Cp_0A_p/c^* \tag{10}$$

Because the burning area is $A_b = \pi DL$ and the throat area is equal to the port area $A_p = \pi D^2/4$, the burning-to-throat area ratio is

$$A_b/A_p = 4L/D \tag{11}$$

When using the assumption of a uniform instantaneous burning rate $\dot{r}$ [Eq. (1)], as well as the steady-state approximation, the instantaneous head pressure is

$$p_0 = [\rho_p ac^*(4L/CD)]^{1/(1-n)} = p_{0i}(D_i/D)^{1/(1-n)} \tag{12}$$

which is higher by a factor of $(1/C)^{1/(1-n)}$, for example, by 56% for $n = 0.5$, than the chamber pressure of a nozzled rocket with a similar burning-to-throat area ratio. Equation (12) reveals that the head pressure $p_0 \propto (L/D)^{1/(1-n)}$. For a similar port diameter, it is always higher for larger grain lengths. Notice that, for a given motor, the maximum pressure $p_{\max}$ is always obtained at the beginning of the combustion (and, of course, at the motor head end, i.e., $p_{\max} = p_{0i}$), and it would be higher for smaller initial port diameters D_i.

The burning rate, which can be calculated from Eqs. (1) and (12), is also maximal at the beginning. It decreases with the increase in port diameter according to

$$\dot{r} = \dot{r}_i(D_i/D)^{n/(1-n)} \tag{13}$$

The time dependence of the port diameter can be expressed by

$$\frac{dD}{dt} = 2\dot{r} \tag{14}$$

When using Eq. (13) for the instantaneous burning rate and integrating over the range of port diameters from D_i (at $t = 0$) to $D_{\max}$ (at $t = t_b$), the overall burning time can be shown to be

$$t_b = [(1-n)D_i/2\dot{r}]\left[(D_{\max}/D_i)^{1/(1-n)} - 1\right] \tag{15}$$

The average head pressure p_{av} defined as

$$p_{av} = \frac{1}{t_b}\int_0^{t_b} p_0\,dt \tag{16}$$

depends on propellant properties (ρ_p, a, c^*, and n), as well as on geometric parameters (D_i, $D_{\max}$, and L),

$$p_{av} = \left(\frac{1}{1-n}\right)\left(\frac{4\rho_p ac^*}{C}\right)^{1/(1-n)} L^{1/(1-n)} \cdot \left[\frac{\ell n(D_{\max}/D_i)}{D_{\max}^{1/(1-n)} - D_i^{1/(1-n)}}\right]$$

$$= p_{0i}\left(\frac{1}{1-n}\right)\left[\frac{\ell n(D_{\max}/D_i)}{(D_{\max}/D_i)^{1/(1-n)} - 1}\right] \tag{17}$$

Equation (17) shows that $p_{av} \propto L^{1/(1-n)}$, just as are the instantaneous and the maximum pressures. However, the dependence of p_{av} on D_i and $D_{\max}$ is a more complex one, revealing different behavior. The ratio between the average and maximum pressures ($p_{\max} = p_{0i}$) is independent of both L and propellant properties (except n). It does, however, decrease monotonically with increasing the ratio $D_{\max}/D_i$,

$$\frac{p_{av}}{p_{\max}} = \left(\frac{1}{1-n}\right)\left[\frac{\ell n(D_{\max}/D_i)}{(D_{\max}/D_i)^{1/(1-n)} - 1}\right] \tag{18}$$

Note that the burning-rate coefficient a has the same effect as the propellant length L on both $p_{\max}$ and p_{av}. On the other hand, a lower value of n implies smaller variations in pressure during burning and a higher ratio of $p_{av}/p_{\max}$. Such a situation is desirable from the structural design standpoint and, as a general rule, would result in a better motor performance for the same $p_{\max}$.

Because of the specific configuration, the thrust of an NSRM can be determined simply from

$$F = (p_0 - p_a)A_p = p_0A_p - p_aA_p \tag{19}$$

In terms of internal-ballistics parameters, Eq. (19) can be expressed as follows:

$$F = \left(\rho_p ac^* 4L/C\right)^{1/(1-n)}(\pi/4)D^{(1-2n)/(1-n)} - p_a(\pi/4)D^2$$

$$= p_{0i}(\pi/4)D_i^{1/(1-n)}D^{(1-2n)/(1-n)} - p_a(\pi/4)D^2 \tag{20}$$

Equation (20) implies that for $n = \frac{1}{2}$ the first thrust term is constant. For $n < \frac{1}{2}$ it increases with time during burning (as D increases), whereas for $n > \frac{1}{2}$ it decreases with time. The second term, however, always increases with time, that is, with increasing D, for any nonzero p_a. At the beginning its magnitude is very small compared to the main thrust term. However, toward the end of the motor operation it may increase substantially and cannot be neglected.

A constant thrust (neutral operation) throughout the burning is an exact mathematical solution for $n = \frac{1}{2}$ only when $p_a = 0$ (vacuum operation). However, for any nonzero p_a, a close to neutral operation would generally be characterized by $n < \frac{1}{2}$, yielding an initial increase of thrust with time followed by a monotonic decrease after attaining a peak value.

The instantaneous specific impulse is defined as

$$I_{sp} = F/\dot{m}g_0 \tag{21}$$

When substituting Eqs. (10) and (19) in Eq. (21), the instantaneous specific impulse can be expressed by common specific characteristics,

$$I_{sp} = \left(c^*/Cg_0\right)[1 - (p_a/p_0)] = C_Fc^*/g_0 \tag{22}$$

where the instantaneous thrust coefficient is

$$C_F = (1/C)[1 - (p_a/p_0)] \tag{23}$$

Equation (23) shows that at any instant the thrust coefficient $C_F \leq 1/C$ (the equality is valid for vacuum operation). With C constant and equal to approximately 0.8 [Eq. (4)], C_F of an NSRM is always lower than about 1.25 (compared to typical values of the order of 1.5–1.6 for nozzled rockets). Note that when C_F is related to the head-end pressure, it is expressed as

$$C_F = F/(Cp_0A_p) \tag{24}$$

Because the operating conditions of a nozzleless motor vary continuously, the mean specific impulse based on the total impulse and the overall propellant mass consumed is of interest:

$$\bar{I}_{sp} = \frac{\int_0^{t_b} F\,dt}{g_0 \int_0^{t_b} \dot{m}\,dt} = \frac{\int_0^{t_b} F\,dt}{m_p g_0} \tag{25}$$

where m_p is the overall propellant mass

$$m_p = (\pi \rho_p L/4)\left(D_{max}^2 - D_i^2\right) \tag{26}$$

When transforming from time to port diameter variations [see Eq. (15)]

$$dt = \left[1/2\dot{r}_i D_i^{n/(1-n)}\right] D^{n/(1-n)}\,dD \tag{27}$$

and integrating from D_i to D_{max}, one obtains after algebraic arrangement

$$\bar{I}_{sp} = \frac{c^*}{Cg_0}\left\{1 - \frac{p_a}{p_{0i}} \cdot \frac{2-2n}{3-2n} \cdot \frac{(D_{max}/D_i)^{(3-2n)/(1-n)} - 1}{(D_{max}/D_i)^2 - 1}\right\} \tag{28}$$

The corresponding average thrust coefficient that is derived from

$$\bar{C}_F = \bar{I}_{sp} g_0/c^* \tag{29}$$

is

$$\bar{C}_F = \frac{1}{C}\left\{1 - \frac{p_a}{p_{0i}} \cdot \frac{2-2n}{3-2n} \cdot \frac{(D_{max}/D_i)^{(3-2n)/(1-n)} - 1}{(D_{max}/D_i)^2 - 1}\right\} \tag{30}$$

For performance evaluation, it is often advisable to compare the average specific impulse achievable in a nozzleless rocket to the corresponding specific impulse of an adapted nozzle rocket operating at a constant chamber pressure equal to the nozzleless motor average head pressure p_{av}. It is easy to see that

$$\bar{I}_{sp,NL}/I_{sp,N} = \bar{C}_{F,NL}/C_{F,N}^{\circ} \tag{31}$$

Generally, C_F° is expressed by

$$C_F^{\circ} = \Gamma\sqrt{[2\gamma/(\gamma-1)]\left[1 - (p_e/p_c)^{(\gamma-1)/\gamma}\right]} \tag{32}$$

where p_e is the exit pressure, which is equal to the ambient pressure ($p_e = p_a$) in the case of the adapted nozzle, and p_c is the stagnation chamber pressure. By the using of $p_c = p_{av}$ and $p_e/p_c = (p_e/p_{max})(p_{max}/p_{av})$, one obtains for the nozzled rocket

$$C_F^{\circ} = \Gamma\sqrt{\frac{2\gamma}{\gamma-1}} \times \left[1 - \left(\frac{p_a}{p_{max}} \cdot (1-n) \cdot \frac{(D_{max}/D_i)^{1/(1-n)} - 1}{\ln(D_{max}/D_i)}\right)^{(\gamma-1)/\gamma}\right]^{\frac{1}{2}} \tag{33}$$

It is straightforward to show that the ratio between the nozzleless $\bar{C}_F$ and the nozzled C_F° gets its extreme values for the following conditions: The lowest ratio is associated with infinitesimally small ambient-to-maximum pressure ratio, that is, either vacuum operation or extremely high initial chamber pressure,

$$\min\left(\bar{C}_F/C_F^{\circ}\right) \qquad \text{for} \qquad (p_a/p_{max}) \to 0 \tag{34}$$

Note that the minimum ratio is obtained when both $\bar{C}_F$ and C_F° get their maximum values,

$$\bar{C}_F = 1/C, \qquad C_F^{\circ} = \Gamma\sqrt{2\gamma/(\gamma-1)}$$

$$\min\left(\bar{C}_F/C_F^{\circ}\right) = \sqrt{\gamma^2 - 1}/\gamma \tag{35}$$

For illustration, the corresponding numerical values for $\gamma = 1.2$ are

$$\bar{C}_F = 1.24, \qquad C_F^{\circ} = 2.25, \qquad \min\left(\bar{C}_F/C_F^{\circ}\right) = 0.55$$

The highest ratio will be achieved for the lowest operational pressure and for an infinitesimally thin web. If one presumes that the minimum chamber pressure during the entire operation time should ensure choking conditions, then

$$\max\left(\bar{C}_F/C_F^{\circ}\right) \qquad \text{for} \qquad (D_{max}/D_i) \to 1, \quad p_{av} \to p_{0i} = p_{max}$$

$$p_{max} = (\gamma+1)p_a \tag{36}$$

In this maximum-ratio case, however, both $\bar{C}_F$ and C_F° attain their minimum values, namely, both nozzleless and nozzled rockets exhibit their poorest performance,

$$\bar{C}_F = \frac{1}{C} \cdot \frac{\gamma}{\gamma+1}, \qquad C_F^{\circ} = \Gamma\sqrt{\frac{2\gamma}{\gamma-1}}\left[1 - \left(\frac{1}{\gamma+1}\right)^{(\gamma-1)/\gamma}\right]^{\frac{1}{2}}$$

$$\max \frac{\bar{C}_F}{C_F^{\circ}} = \left[\frac{(\gamma-1)}{(\gamma+1)\left\{1 - [1/(\gamma+1)]^{(\gamma-1)/\gamma}\right\}}\right]^{\frac{1}{2}} \tag{37}$$

Again, for $\gamma = 1.2$,

$$\bar{C}_F = 0.68, \qquad C_F^{\circ} = 0.79, \qquad \max \bar{C}_F/C_F^{\circ} = 0.86$$

Note that common operating conditions, e.g., $p_{max}/p_a = 100$, $D_{max}/D_i = 3$, and $n = 0.5$, imply C_F ratio of approximately 0.8.

The range of obtainable $\bar{C}_F/C_F^{\circ}$ ratios (which is equivalent to the range of relative I_{sp} values), as is shown here, demonstrates the great significance of an analytical investigation, which clearly indicates the operational range and can avoid erroneous speculations and extrapolations. For instance, the extrapolated values of relative specific impulse of 90–92%, which are predicted by Ref. 2, are far beyond the possible theoretical limit of 86% that results from the present analysis.

Experimental

A test program was aimed at a parametric study of the influence of design factors on the motor performance to examine the theoretical analysis and to enhance the database.

In general, tests were performed with a propellant grain having a straight circular port. Regularly, the grain outer-to-inner-diameter ratio is limited to 3–3.5. Application of a stress-relief-liner (SRL) technology enabled the extension of the grain outer-to-inner-diameter ratio to values otherwise prohibited by thermal stresses, when compared to regular liner technology. The propellant grain was restriction free at both fore and aft ends. The propellant used was a nonmetallized hydroxyl-terminated-polybutadiene (HTPB)-based formulation containing 84.5% ammonium perchlorate (AP) oxidizer of a trimodal particle distribution (180/8/2μ). The propellant exhibited a relatively high burning rate (30 mm/s at 10 MPa) with a pressure exponent of approximately 0.5 and $\gamma = 1.2$. The motor casing consisted of a thick-walled steel tube with an inner diameter of 103 mm and a variable length. Ignition

was accomplished by a pyrotechnic igniter consisting of 6 grams of a boron/potassium-nitrate (BPN) powder located within a cavity in the forward closure.

Continuous measurements of the static pressure within the propellant port during burning in different cross sections along the grain were conducted in a number of tests through radial holes in the propellant web, using a special technique. The holes were formed by 7.8-mm pins that were inserted radially into the combustion chamber before the propellant casting process. After casting and curing, the pins were withdrawn, thus forming ports passing through the web. The inner surfaces of the ports were coated by a 2.1-mm-thick cast liner layer, leaving holes with a 3.6-mm diam. Other ports along the motor case (nonprotruding into the grain) were used to detect pressure jumps, indicating local web burnout. Head-end pressure and motor thrust were the two main motor performance variables measured. All pressure and thrust measurements were carried out by BLH strain-gauge transducers with an accuracy of $\pm 1\%$. A computerized data acquisition and processing system with sampling rates between 400 and 3000 samples/s was applied.

Several geometric grain design parameters were systematically varied to investigate their effects on motor performance. Motor case inner diameter, equal to the propellant maximum diameter D_{max}, was kept constant (103 mm) during this study. The effect of motor length-to-diameter ratio L/D_{max} was investigated by firing motors with different ratios (3.5, 4.5, 5, 6, 7, 10.5, 11.5, and 12.5). The effect of the grain loading factor λ, defined as the grain outer-to-inner-diameter ratio D_{max}/D_i, was studied in test firings of motors with four different nominal inner grain diameters (17.3, 20.8, 26.0, and 38.4 mm) that correspond to λ of approximately 6, 5, 4, and 2.7, respectively, for most of the L/D_{max} ratios. Actual inner diameters could be larger than the nominal values by as much as 5% due to propellant shrinkage during curing.

The effect of an aft-end cone geometry (initial expansion ratio and divergence half-angle) on motor performance was investigated by a limited number of firing tests.

Most of the firing tests were performed at ambient temperatures of 25 ± 5°C. Motor performance temperature sensitivity was studied by additional tests conducted at conditioning temperatures of -10°C and $+65$°C.

Results and Discussion

The validity of the assumption of a uniform burning rate along the grain was directly tested by determining the local web burnout instants along the motor from pressure jumps detected by pressure transducers connected to the inner case surface on exposure to the chamber conditions (Fig. 2). The burning time of the head-end section was found to be shorter by approximately 10% than that of the downstream section, indicating that the average burning rate at the head end was higher by the same order. This is a relatively small deviation from the uniform burning-rate assumption, particularly when taking into account that the burning time is much affected by the low burning rate at the latest stage (when $\dot{r}$ is relatively low). For this propellant, if the burning rate were only pressure dependent, the burning rate at the head end would be about 50% higher [i.e., ratio of $(\gamma + 1)^n$] than in the downstream section.

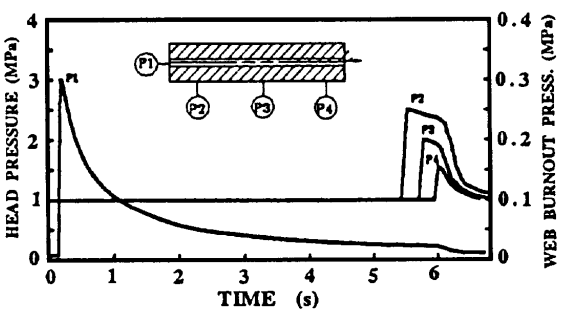

Fig. 2 Web burnout times at different axial locations indicating the relative regression rates.

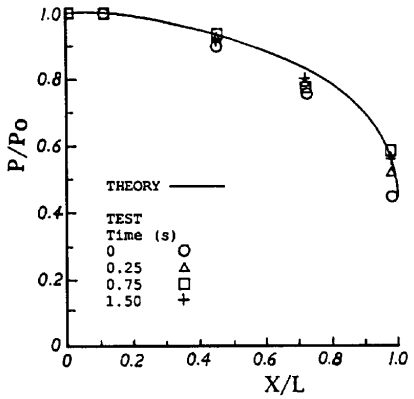

Fig. 3 Static-to-head-end pressure ratio along the motor: L = 1083 mm, D_i = 38.4 mm, t_b = 1.8 s, and γ = 1.2.

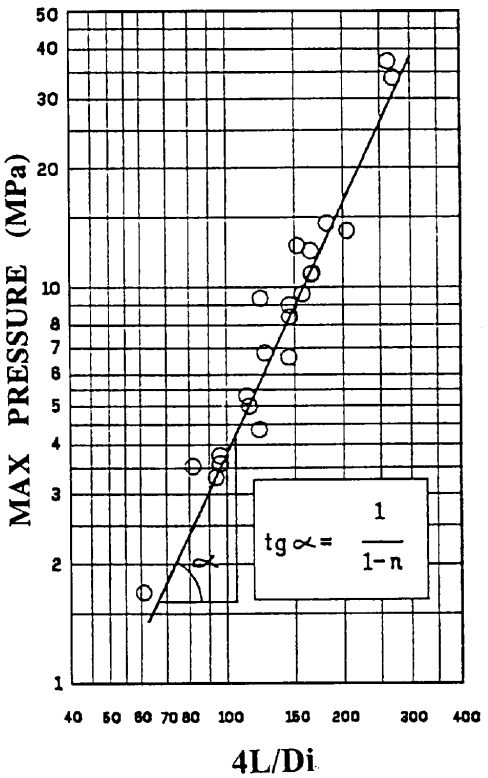

Fig. 4 Test data of p_{max} vs L/D_i.

The usefulness of the one-dimensional analysis for the prediction of main flow properties in the nozzleless motor can be demonstrated from the experimental results of the variation of static pressure to head-end pressure ratio along the grain. The agreement with the one-dimensional theory, which assumes a uniform burning rate along the grain [Eq. (6)], is very good (Fig. 3), as is also indicated by Ref. 8. In fact, with the typical spread of motor test results, it would be impractical to detect second-order effects (such as two-dimensional influences).

Figure 4 shows test results of the maximum pressure ($p_{max} = p_{0i}$) vs the length-to-initial-port-diameter ratio for different motor geometries ranging for p_{max} from 1.5 to 35 MPa and for L/D_i from 15 to 75. As predicted by the theory [Eq. (12)], the test results were very well correlated by a straight line on a log-log plot with a slope of 2.1, indicating a pressure exponent of 0.52, in an excellent agreement with the independently measured value of n (in a strand burner). Figure 4 points out and supports the following: First, the quasi-steady-state assumption leading to the instantaneous pressure calculation is generally correct. Second, one-dimensional flow with choking conditions at the downstream end is a reasonable description. Third, the assumption of a uniform burning rate along

the grain, which can be described by a constant exponent of the head-end pressure, is a good physical approximation (resulting, as stated before, from the compensating effects of pressure and erosive burning contributions). If the burning-rate behavior along the grain was different, Fig. 4 would exhibit a different dependence.

The substantial decrease in head-end pressure during typical nozzleless motor operations is shown in Fig. 5 for a range of motor lengths (527–1083 mm) and initial port diameters (17.3–38.4 mm) by presenting the burnout-to-initial-head-pressure ratio. The experimental results are in agreement with the theory [Eq. (12)], predicting $p_{0b}/p_{0i} = (D_{max}/D_i)^{-1/(1-n)}$ with no effect of motor length. The theoretical line is drawn for $n = 0.5$.

The strong effect of motor length on initial head pressure (according to $1/1-n$ exponent), as predicted by Eq. (12), is shown in Fig. 6, with the initial port diameter as a parameter (whose influence is according to $-1/1-n$ power).

Having both p_{max} and p_{av} the same dependence on the grain length, that is, relative to $L^{1/(1-n)}$ [see Eqs. (12) and (17)], should yield a linear proportion between p_{av} and p_{max} for each value of D_i, independently of L, where the proportionality factor is only a function of the diameter ratio (and n). Figure 7 reveals this behavior for a variety of tests, covering grain lengths from 370 to 1200 mm, in excellent agreement with theoretical lines drawn for $n = 0.5$. Increasing the average pressure by increasing the grain length L implies the same relative increase in the maximum pressure p_{max}.

Equations (12) and (17) reveal that when decreasing D_i both p_{max} and p_{av} increase. However, whereas p_{max} is proportional to $D_i^{-1/(1-n)}$ and, hence, rapidly increases with decreasing the initial diameter, p_{av} is approximately relative to $\ell n(1/D_i)$ for small values of D_i and a fixed value of D_{max}, and thus, its growth with decreasing D_i is very moderate. This trend is generally shown in Fig. 7, showing larger slopes in the p_{av} vs p_{max} plot for larger D_i values. The ratio

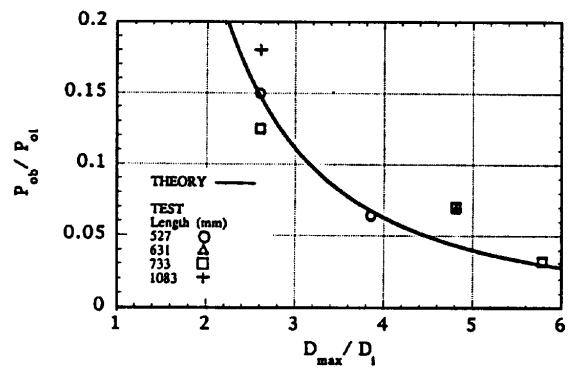

Fig. 5 Comparison between theory and experiment of burnout-to-initial-head-end pressure ratio.

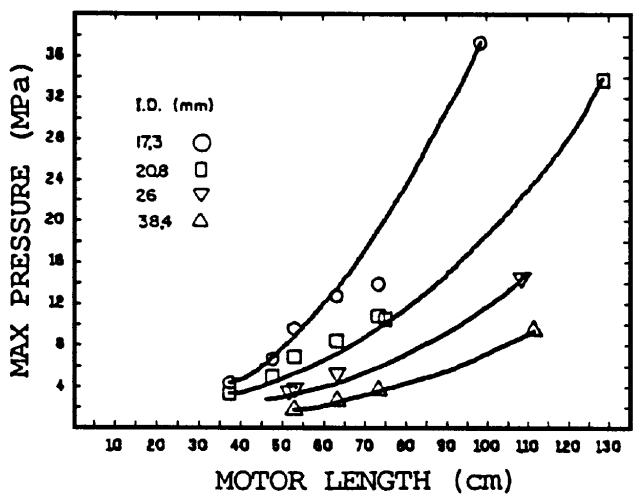

Fig. 6 Maximum head pressure vs motor length with D_i as a parameter.

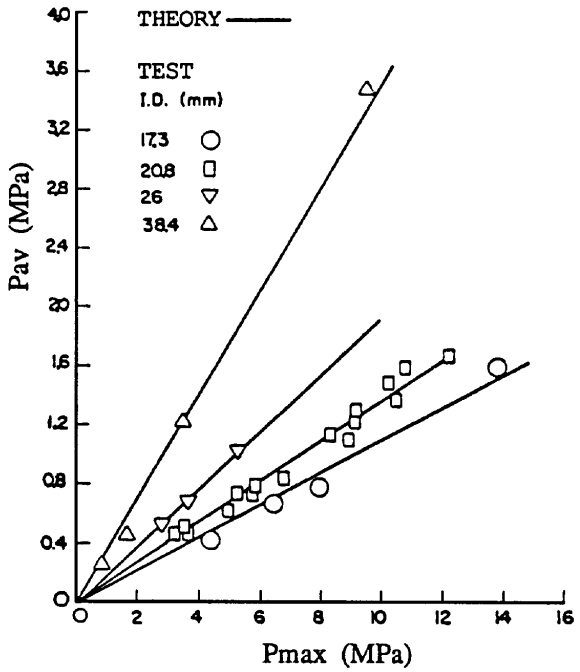

Fig. 7 p_{av} vs p_{max} with D_i as a parameter.

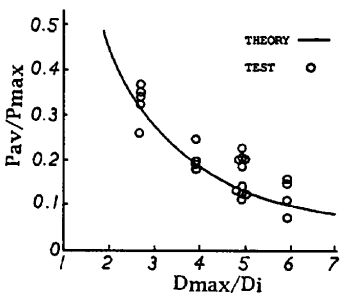

Fig. 8 Comparison between experimental data and theory: p_{av}/p_{max} vs D_{max}/D_i.

p_{av}/p_{max} that is expressed by Eq. (18) reveals a mere dependence on D_{max}/D_i with no effect of propellant properties or length. Figure 8 shows good agreement between the experimental results and this theoretical prediction. Figure 8 also shows that if the increase of average pressure is accomplished via decreasing the initial diameter (to increase overall performance and propellant loading fraction) one pays a penalty of a much higher undesirable increase in the maximum pressure (and, consequently, a decrease in p_{av}/p_{max}), implying a thicker and heavier motor case. On the other hand, a thinner propellant web, that is, smaller D_{max}/D_i, would result in a larger p_{av}/p_{max} ratio, but in lower p_{av} (as well as p_{max}) than for a smaller D_i and in lower propellant loading fraction and overall performance.

As implied by Eq. (28), the specific impulse approaches an asymptotic value when increasing p_{max} or p_{av}. It can be proven that the increase of motor pressure by increasing the grain length (and similarly by increasing the burning-rate coefficient a) has a more beneficial effect on increasing the specific impulse than the same increase in pressure via decreasing the initial port diameter. Lowering the pressure exponent n has an even better influence.

The ratio between the measured specific impulse in different nozzleless firing tests and the theoretical specific impulse of an adapted-nozzle rocket operating at a chamber pressure equal to p_{av} is shown in Fig. 9. The practical ratios obtained lie between 0.73 and 0.82. Possible unchoked operating conditions toward the end of the combustion in low p_{av} cases might have caused some reduction in the actual specific impulse. As stated before, the maximum theoretical specific impulse ratio cannot exceed 0.86.

A commonly used method to enhance the delivered specific impulse is the tapering of the motor aft end, which acts for part of the burning time as an expansion cone and improves kinetic energy recovery. The effect of aft-end geometry was investigated by testing

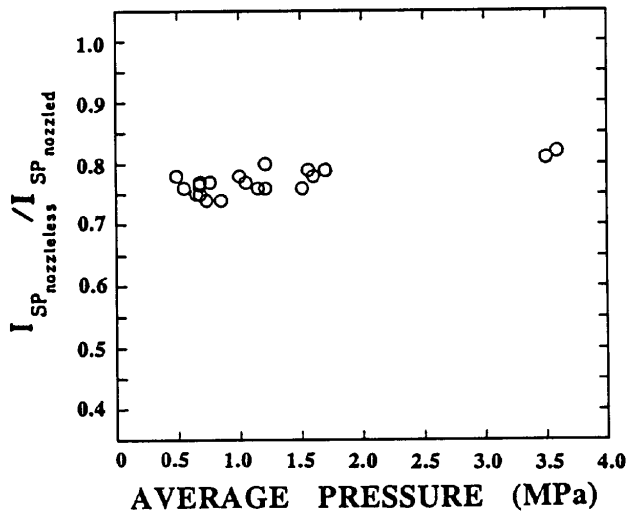

Fig. 9 Test results of nozzleless to nozzled motor specific impulse ratio.

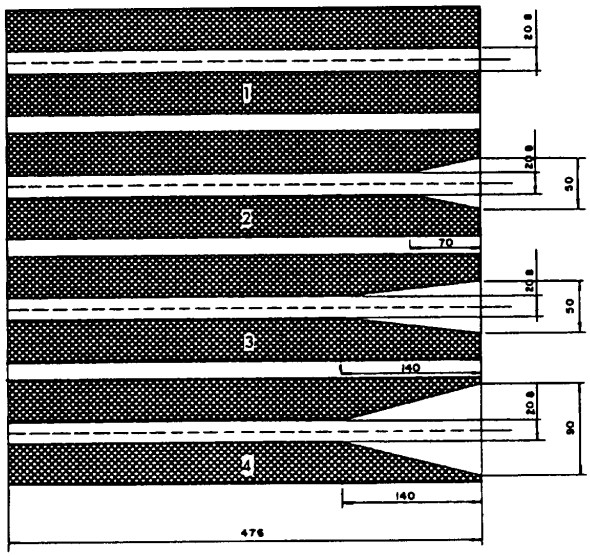

Fig. 10 Aft-end geometries tested.

motors with various cone lengths and expansion angles (Fig. 10). The overall motor length and inner diameter were kept constant. The results obtained show, however, that motor efficiency decreased as cone length increased. This is explained by the reduction of motor average pressure (because of smaller effective burning area) leading to higher I_{sp} losses. An exit cone may improve the performance of nozzleless motors, where the reduction of burning area by the expansion cone is insignificant relative to the overall burning area. In the motors tested this condition was not valid.

From the analysis of the results obtained from tests at three different conditioning temperatures and two motor lengths, it became evident that nozzleless motors are less temperature sensitive than the nozzled motors. Results from this study indicate temperature sensitivity of the motor pressure to be 0.15–0.20%/K, whereas data obtained from nozzled motor firings with an identical propellant formulation revealed a sensitivity factor of 0.3%/K. This result is in good agreement with data obtained by other investigators.[2,11] The mechanism for this phenomenon is associated with the change of grain inner bore diameter due to pressure stresses (grain deflection) and that the bore diameter determines the choking cross section. Because the propellant modulus of elasticity decreases with temperature, larger deformations of the inner bore diameter (larger throat area) occur at high conditioning temperatures, compensating for the increase in burning rate due to temperature effect. At low conditioning temperatures, the increased propellant stiffness results in a smaller deformation of the grain port, reducing the relative temperature effect on the burning rate. Also note that grain deformation may be particularly noticeable at the initial burning stage, causing enlargement of the bore and consequently some decrease in the actual p_{max} and an apparent increase in thrust when calculated on the basis of the measured head pressure and initial nominal bore diameter. This was recognized in the tests, but was not accounted for in the model.

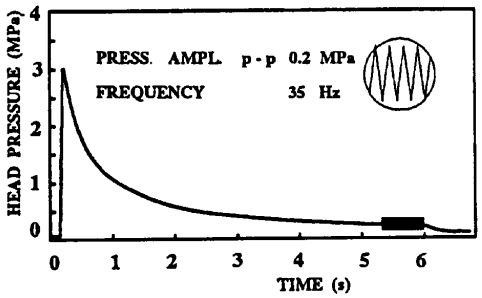

Fig. 11 Instability detected during motor firing.

Low-frequency (about 35-Hz) pressure oscillations were observed during the final combustion stages of some firing tests (see Fig. 11). This phenomenon, which has also been observed by other investigators,[11] is usually referred to as L^* (bulk) instability. However, our observations reveal that the oscillation frequency obtained is much lower (approximately by an order of magnitude) than the classical L^*-instability frequency, that is expressed by the inverse of the residence time,

$$f_{L^*} = \Gamma^2 c^*/L^* \tag{38}$$

and is similarly far from any motor acoustic instability mode. L^*, which is defined as the ratio between the combustor volume and throat area, is actually the motor length in the case of a nozzleless rocket. In the present tests instability was observed only for motor lengths less than 630 mm and for pressure levels below 0.3 MPa (on average 0.26 MPa). It was also found that increased propellant conditioning temperature (65°C) caused stable combustion in motors that otherwise exhibited unstable operation. A similar effect was caused by the addition of a high-expansion-ratio exit cone when maintaining the same chamber pressure. On the other hand, reduced burning-rate propellants generated instability in motors that showed stable operation with the regular propellant. It is suspected that these observations indicate that the main trigger for pressure oscillations is the interaction between the port flow and the ambient atmosphere at unstable choking conditions, when the aft-end pressure becomes too low and the operating regime is close to a transition to unchoked flow.

Conclusions

The usefulness of analytical modeling of the internal ballistics of nozzleless solid-propellant rocket motors for revealing the fundamental operating characteristics has been demonstrated. The quasi-steady-state one-dimensional analysis of the port flow has yielded closed-form expressions for major operating parameters. One very significant conclusion resulting from the analysis is that the maximum theoretical obtainable specific impulse of a nozzleless motor (with no exit cone) is limited to approximately 86% of its value in an adapted-nozzle rocket operating at the same average chamber pressure. This theoretical finding contradicts speculated and extrapolated values as high as 92% quoted in the literature on the basis of empirical correlations.

Other main results that exhibit good agreement between the theoretical analysis and data from a parallel experimental effort follow.

The simplified assumption of a uniform overall burning rate along the propellant grain is a realistic first-order physical approximation accounting for the compensating contribution of erosive burning to the decreasing pressure-dependent burning rate contribution in the downstream section due to reduced local pressure.

Within the experimental spread, a one-dimensional flow analysis describes well the pressure ratio along the port, when assuming $M_e = 1$.

The average-to-maximum pressure ratio is independent of grain length and propellant properties including the burning-rate coefficient a. Increasing L and a is a reasonable way to increase average pressure and specific impulse. Decreasing n may be even a better way because it increases p_{av}/p_{max}. However, increasing the diameter ratio D_{max}/D_i implies a penalty of reducing p_{av}/p_{max} (in a well-predicted manner), although it enables higher propellant loading fractions.

Forming an exit cone at the aft end of the grain may improve the motor performance only if the loss of effective burning area is relatively small. L/D_{max} of 4.7 was found to be too small, causing a decrease in performance when using an exit cone.

Because of the strong coupling between bore diameter and internal ballistics, temperature sensitivity of chamber pressure in nozzleless motors was found to be smaller than for nozzled rockets due to grain deformation. Grain deformation may also have a noticeable effect on the initial pressure and thrust.

Finally, low-frequency combustion instability seems to be triggered by unstable choking conditions, when the motor pressure drops to a low value close to transition to unchoked flow conditions. Note that the observed frequency does not correspond to that of the so-called L^* (bulk) instability.

References

[1]Timnat, Y. M., *Advanced Chemical Rocket Propulsion*, Academic Press, London, 1987, Chap. 6, pp. 107–118.

[2]Procinsky, I. M., and McHale, C. A., "Nozzleless Boosters for Integral-Rocket-Ramjet Missile Systems," *Journal of Spacecraft and Rockets*, Vol. 18, No. 3, 1981, pp. 193–199.

[3]Price, E. W., "One-Dimensional, Steady Flow with Mass Addition and the Effect of Combustion Chamber Flow on Rocket Thrust," *Jet Propulsion*, Vol. 25, No. 2, 1955, pp. 61–66, 78.

[4]Zucrow, M. J., and Hoffman, J. D., *Gas Dynamics*, Wiley, New York, 1976, Chap. 9, pp. 461–473.

[5]Beddini, R. A., "Analysis of Injection-Induced Flows in Porous Walled Ducts with Application to the Aerothermochemistry of Composite Propellants," Ph.D. Thesis, Rutgers Univ., New Brunswick, NJ, Oct. 1981.

[6]Glick, R. L., and Orr, C. E., "On the Idealized Performance of Nozzleless Rocket Motors," AIAA Paper 80-1137, June/July 1980.

[7]Glick, R. L., "On the Performance of Nozzleless Rocket Motors," AIAA Paper 83-1318, June 1983.

[8]Traineau, J.-C., Hervat, P., and Kuentzmann, P., "Cold Flow Simulation of a Two-Dimensional Nozzleless Solid Rocket Motor," AIAA Paper 86-1447, June 1986.

[9]King, M. K., "Consideration of Two-Dimensional Flow Effects on Nozzleless Rocket Performance," *Journal of Propulsion and Power*, Vol. 3, No. 3, 1987, pp. 194, 195.

[10]Balakrishnan, G., Linan, A., and Williams, F. A., "Rotational Inviscid Flow in Laterally Burning Solid-Propellant Rocket Motors," *Journal of Propulsion and Power*, Vol. 8, No. 6, 1992, pp. 1167–1176.

[11]Nahon, S., "Nozzleless Solid-Propellant Rocket Motors: Experimental and Theoretical Investigations," AIAA Paper 84-1312, June 1984.

[12]Traineau, J.-C., and Kuentzmann, P., "Some Measurements of Solid-Propellant Burning Rates in Nozzleless Motors," AIAA Paper 84-1469, June 1984.

[13]Aharon, I., Fuchs, M. D., Timnat, Y. M., and Gany, A., "An Experimental Study on the Effects of Design Parameters on Nozzleless Rocket Motor Performance," *29th Israel Conference on Aviation and Astronautics*, Collection of Papers, Feb. 1987, pp. 9–15.

[14]Yamada, K., Goto, M., and Ishikawa, N., "Simulative Study on the Erosive Burning of Solid Rocket Motors," *AIAA Journal*, Vol. 14, No. 9, 1976, pp. 1170–1176.

[15]Beddini, R. A., "Reactive Turbulent Boundary-Layer Approach to Solid-Propellant Erosive Burning," *AIAA Journal*, Vol. 16, No. 9, 1978, pp. 898–905.

[16]Beddini, R. A., "Aerothermochemical Analysis of Erosive Burning in a Solid-Propellant Rocket Motor," *AIAA Journal*, Vol. 18, No. 11, 1980, pp. 1347–1353.

[17]King, M. K., "Prediction of Solid Propellant Burning Rates in Nozzleless Motors," AIAA Paper 82-1200, June 1982.

[18]Razdan, M. K., and Kuo, K. K., "Turbulent Flow Analysis of Erosive Burning of Cylindrical Composite Solid Propellants," *AIAA Journal*, Vol. 20, No. 1, 1983, pp. 122–128.

[19]Mikkelsen, C. D., and Roys, G. P., "Applications of the Saderholm Erosive Burning Model to Nozzleless Solid Propellant Rocket Motors," *Journal of Spacecraft and Rockets*, Vol. 21, No. 1, 1984, pp. 41–46.

[20]Murray, J. W., Mikeska, A. J., and Tonkin, M. E., "NPP Grain Deflection Model," AIAA Paper 82-1201, June 1982.

[21]King, M. K., "Prediction of Metal Combustion Efficiency in Low Port-to-Throat Area Ratio and Nozzleless Solid Rocket Motors," AIAA Paper 82-1202, June 1982.

[22]Harry, D. P., "Status of Nozzleless Solid Motor Internal Ballistics Analysis," AIAA Paper 77-910, July 1977.

[23]Procinsky, I. M., and Yezzi, C. A., "Nozzleless Performance Program," AIAA Paper 82-1198, June 1982.

[24]Coats, D. E., Dang, L., and Nickerson, G. R., "Interior Ballistics Calculations for Nozzleless Solid-Propellant Rocket Motors," AIAA Paper 82-1199, June 1982.